



Cite this: *Phys. Chem. Chem. Phys.*,  
2017, 19, 22528

# Nonlinear behavior and fluctuation-induced dynamics in the photosensitive Belousov–Zhabotinsky reaction

Valérie Voorsluijs,<sup>id</sup>\*<sup>ab</sup> Ioannis G. Kevrekidis<sup>c</sup> and Yannick De Decker<sup>ab</sup>

The photosensitive Belousov–Zhabotinsky (pBZ) reaction has been used extensively to study the properties of chemical oscillators. In particular, recent experiments revealed the existence of complex spatiotemporal dynamics for systems consisting of coupled micelles ( $V < 10^{-21}$  L) or droplets ( $V \approx [10^{-8}–10^{-11}]$  L) in which the pBZ reaction takes place. These results have been mostly understood in terms of reaction–diffusion models. However, in view of the small size of the droplets and micelles, large fluctuations of concentrations are to be expected. In this work, we investigate the role of fluctuations on the dynamics of a single droplet with stochastic simulations of an extension of the Field–Körös–Noyes (FKN) model taking into account the photosensitivity. The birhythmicity and chaotic behaviors predicted by the FKN model in the absence of fluctuations become transient or intermittent regimes whose lifetime decreases with the size of the droplet. Simple oscillations are more robust and can be observed even in small systems ( $V > 10^{-12}$  L), which justifies the use of deterministic models in microfluidic systems of coupled oscillators. The simulations also reveal that fluctuations strongly affect the efficiency of inhibition by light, which is often used to control the kinetics of these systems: oscillations are found for parameter values for which they are supposed to be quenched according to deterministic predictions.

Received 16th May 2017,  
Accepted 2nd August 2017

DOI: 10.1039/c7cp03260a

rsc.li/pccp

## 1 Introduction

Since its discovery in the early 1960s, the Belousov–Zhabotinsky (BZ) reaction has been extensively studied (see ref. 1 and references therein) and is now considered as the chemical oscillatory reaction *par excellence*. The first mechanism for this reaction has been proposed by Field, Körös and Noyes in 1972<sup>2,3</sup> and many simplified versions of the model (*e.g.* the Oregonator<sup>4</sup>) have been developed. The BZ reaction is now known to generate a wide range of complex behaviors not only in aqueous solutions, but also in gels,<sup>5–8</sup> membranes,<sup>9,10</sup> microemulsions<sup>8,11–18</sup> or microfluidic assemblies.<sup>8,18–25</sup> Even the simplest configuration, consisting in a stirred batch reactor, can display periodic oscillations, transient quasiperiodicity<sup>26</sup> or chaos.<sup>26,27</sup> In a continuous stirred tank reactor (CSTR), the observed behaviors include bistability,<sup>28,29</sup> multiperiodic oscillations and sustained quasiperiodicity and chaos.<sup>30</sup> In spatially extended systems, the coupling between reaction and diffusion

gives rise to a wealth of patterns and waves, including target-like patterns.<sup>31</sup>

The most exotic reaction–diffusion patterns are found in the reverse (water-in-oil) BZ-AOT microemulsion system.<sup>11,12</sup> Stationary Turing structures,<sup>14,32</sup> accelerating waves,<sup>14</sup> spirals and antispirals,<sup>33</sup> packet waves,<sup>34</sup> segmented waves,<sup>35</sup> stationary and oscillatory localized structures (oscillons),<sup>36</sup> jumping waves, bubble waves and rotating waves<sup>37</sup> were for example observed. In this system, the aqueous reacting solution is encapsulated in micelles and dispersed into a continuous phase of octane. The micelles are stabilized by sodium bis(2-ethylhexyl)sulfosuccinate, a surfactant also known as aerosol OT (AOT) and the radius of the water core is  $R_w \approx 0.17\omega$  nm, where  $\omega = [\text{H}_2\text{O}]/[\text{AOT}]$  is the ratio of concentrations of water and surfactant. Transitions between the aforementioned behaviors occur when the concentrations and the volume fraction  $\phi_d$  of the dispersed phase (water and surfactant) are varied. Most of the BZ reactants are polar species and thus tend to be confined in the aqueous core of the micelles. However, some nonpolar intermediates like  $\text{Br}_2$  and  $\text{BrO}_2^\bullet$  are also generated by the reaction and are likely to move to the surfactant layer or the hydrophobic phase, where they can diffuse and eventually enter another micelle. Mass exchange between micelles is also ensured by a collision–coalescence–redispersion mechanism specific to microemulsions.<sup>18</sup> The BZ-AOT micelles can thus be viewed as a population of coupled,

<sup>a</sup> Center for Nonlinear Phenomena and Complex Systems (CENOLI),  
Université libre de Bruxelles (ULB), Campus Plaine, C.P. 231, B-1050 Brussels,  
Belgium. E-mail: vvoorslu@ulb.ac.be

<sup>b</sup> Nonlinear Physical Chemistry Unit, Université libre de Bruxelles (ULB),  
Campus Plaine, C.P. 231, B-1050 Brussels, Belgium

<sup>c</sup> Department of Chemical and Biological Engineering and PACM, Princeton University,  
Princeton, NJ 08544, USA

heterogeneous microoscillators. Similar systems of coupled chemical microoscillators have been shown to display interesting collective behaviors<sup>38–43</sup> and constitute very useful models to gain insight into the complex synchronization phenomena taking place in large and heterogeneous populations of biological entities.<sup>44</sup>

So far, the various patterns found in the BZ-AOT system have been described by reaction–diffusion equations. The microemulsion is treated as a continuous medium on the basis that the average time between two micellar collisions is  $\approx 1$  ms, which is much smaller than the period of oscillations.<sup>18</sup> The first models relied on the 2- or 3-variable Oregonator model augmented by additional variables corresponding to the concentrations of  $\text{BrO}_2^\bullet$  and/or  $\text{Br}_2$  in the hydrophobic phase. More recently, a new model was derived from the full Field–Körös–Noyes mechanism in order to reproduce the jumping waves and bubble waves that could not be obtained with previous approaches.<sup>45</sup> This model includes the interaction of light with a photosensitive catalyst, which is used in the preparation of BZ-AOT memory devices<sup>46</sup> or other BZ systems like microfluidic droplets. However, none of the aforementioned approaches accounts for the substantial fluctuations of concentrations that are to be expected in individual micelles. Since the radius of the water core is generally comprized between 2 and 3 nanometers ( $\omega \approx 15$ ), the volume of a single micelle is approximately  $10^{-21}$ – $10^{-22}$  L. Assuming a concentration of 1 M of a given intermediate, a micelle contains about 60 to 600 molecules of this species. Since the concentration of the catalyst is typically in the range of 0.3–0.4 M, the number of particles of this species is even lower. Intrinsic fluctuations are thus expected to be significant and to strongly impact the chemical dynamics in a micelle. In this context, the only study on the role of intrinsic fluctuations in such systems appears to be a work by Vanag, who analyzed the dynamics of coupled BZ micro-oscillators with cellular automata.<sup>47</sup> He showed that some behaviors of the BZ-AOT microemulsions, like the frequency-multiplying bifurcation,<sup>48</sup> could be directly related to the intrinsic fluctuations inside the micelles. However, these investigations were performed with a simplified limit of the full mechanism (the 3-variable Oregonator) and did not include the interaction of light with the photosensitive catalyst. Previous works have also considered external noise. In these cases, the system was submitted to stochastic modulations of the electric field,<sup>49,50</sup> light,<sup>51–54</sup> flow rate<sup>52,55</sup> or temperature.<sup>56</sup>

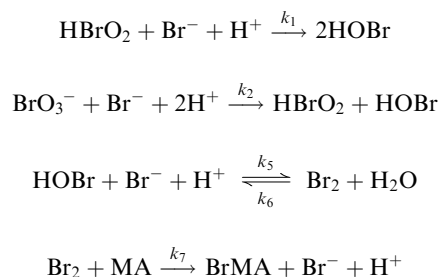
In this work, we investigate the dynamics of the Belousov–Zhabotinsky reaction in a single micelle as predicted by a stochastic implementation of the full FKN model, in which we also incorporate the photoinhibition of the catalyst. The mechanism and the related deterministic evolution equations are given in Section 2. In Section 3, we present the deterministic results obtained by numerical integrations of the model. We show that in some regions of parameter space, the system undergoes a succession of bifurcations leading to multiperiodic oscillations and to chaos, which is consistent with experimental observations.<sup>26,27,57</sup> We also discuss the possibility of observing birhythmicity. In Section 4, we investigate the influence of

intrinsic fluctuations on the chemical dynamics of the system by performing Gillespie simulations corresponding to an extension of the FKN model taking into account the photosensitivity of the reaction (pFKN model). The stochastic realizations exhibit significant deviations with respect to the deterministic trajectories, especially in the chaotic and birhythmic regions. Moreover, the efficiency of photoinhibition is significantly reduced. These effects are observed in droplets whose size is comparable to the water core of micelles, but also in much larger droplets. We summarize the main results of this study and discuss possible future work in Section 5.

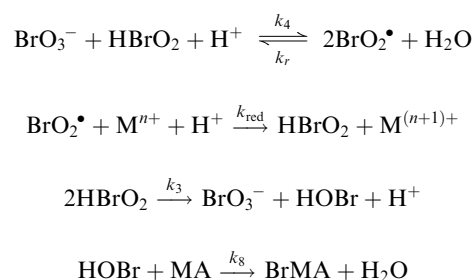
## 2 The Field–Körös–Noyes model

The overall BZ reaction corresponds to the bromination of malonic acid by bromate in an acidic medium. By rationalizing the thermodynamic and kinetic data available for the reactions between bromine, organic and cerium species,<sup>3</sup> Field, Körös and Noyes developed a mechanism that can be decomposed in three processes:

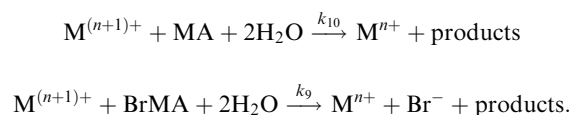
Process A



Process B



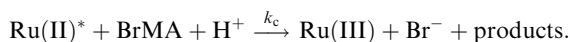
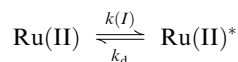
Process C



In Process A, malonic acid ( $\text{MA} \equiv \text{CH}_2(\text{COOH})_2$ ) reacts with bromine to give bromomalonic acid ( $\text{BrMA} \equiv \text{BrCH}(\text{COOH})_2$ ). At this stage,  $\text{HBrO}_2$  is present in small quantities and is exclusively involved in the oxidation of bromide. In this process, bromide is consumed and its concentration decreases until it reaches a critical value  $[\text{Br}^-]_{\text{crit}}$ . Below this concentration, the oxidation of bromide is no longer the dominant reaction and the autocatalysis

of HBrO<sub>2</sub> takes control (Process B). Oxidation of the redox catalyst (M<sup>n+</sup>) also takes place and when the reduced form is almost depleted, the autocatalysis stops. Process C is then enabled and this last process regenerates the reduced catalyst as well as bromide. Once the accumulation of bromide is sufficient, Process A starts again.

Different ions and metallic complexes have been used to catalyze the reaction<sup>1</sup> such as Ce<sup>3+</sup>, Mn<sup>2+</sup>, [Fe(phen)<sub>3</sub>]<sup>2+</sup> (ferroin) or [Fe(bpy)<sub>3</sub>]<sup>2+</sup>.<sup>58</sup> In the presence of a photosensitive catalyst like [Ru(bpy)<sub>3</sub>]<sup>2+</sup>, the oscillations can be inhibited or activated by light.<sup>59</sup> In this work, we will exclusively consider photoinhibition. According to the following mechanism,<sup>59</sup> the excited catalyst reacts with BrMA:



The second reaction generates bromide and inhibits the autocatalysis of HBrO<sub>2</sub>. Assuming an ideal system, the deterministic evolution equations corresponding to the pFKN model are thus

$$\frac{dx}{dt} = -k_1xy + k_2y - 2k_3x^2 - k_4x + k_rw^2 + k_{\text{red}}w(c_0 - z) \quad (1)$$

$$\frac{dy}{dt} = -k_1xy - k_2y - k_5yp + k_6u + k_7u + k_9z + \frac{k(I)(c_0 - z)b}{b_c + b} \quad (2)$$

$$\frac{dz}{dt} = k_{\text{red}}w(c_0 - z) - k_9z - k_{10}z + \frac{k(I)(c_0 - z)b}{b_c + b} \quad (3)$$

$$\frac{du}{dt} = k_5yp - k_6u - k_7u \quad (4)$$

$$\frac{dp}{dt} = 2k_1xy + k_2y + k_3x^2 - k_5yp + k_6u - k_8p \quad (5)$$

$$\frac{dw}{dt} = 2k_4x - 2k_rw^2 - k_{\text{red}}w(c_0 - z) \quad (6)$$

where  $x \equiv [\text{HBrO}_2]$ ,  $y \equiv [\text{Br}^-]$ ,  $z \equiv [\text{M}^{(n+1)+}]$ ,  $u \equiv [\text{Br}_2]$ ,  $p \equiv [\text{HOBr}]$ ,  $w \equiv [\text{BrO}_2^*]$ ,  $c_0 \equiv [\text{M}^{(n+1)+}] + [\text{M}^{n+}]$  and  $b_c = k_d/k_c$ . The concentrations  $h \equiv [\text{H}^+]$ ,  $a \equiv [\text{BrO}_3^-]$ ,  $ma \equiv [\text{MA}]$  and  $b = [\text{BrMA}]$  are considered to be constant and have been incorporated in the kinetic constants, whose values are given in Table 1.  $k(I)$  is the rate constant associated with the excitation of Ru(II). Its value depends on spectral properties like the intensity spectrum of the light source, the transmission spectrum of the filters through

**Table 1** Rate constants and simulations parameters, where  $a$ ,  $h$  and  $ma$  are constants and correspond to  $[\text{BrO}_3^-]$ ,  $[\text{H}^+]$  and  $[\text{BrMA}]$ , respectively

$k_1 = 2 \times 10^6 h \text{ M}^{-1} \text{ s}^{-1}$	$k_8 = 9.3 ma \text{ s}^{-1}$
$k_2 = 2h^2 a \text{ s}^{-1}$	$k_9 = b \text{ s}^{-1}$
$k_3 = 3000 \text{ M}^{-1} \text{ s}^{-1}$	$k_{10} = 0.05 ma \text{ s}^{-1}$
$k_4 = 42ha \text{ s}^{-1}$	$k_r = 2 \times 10^8 \text{ M}^{-1} \text{ s}^{-1}$
$k_5 = 5 \times 10^9 h \text{ M}^{-1} \text{ s}^{-1}$	$k_{\text{red}} = 5 \times 10^6 \text{ M}^{-1} \text{ s}^{-1}$
$k_6 = 10 \text{ s}^{-1}$	$b = 0.1 ma \text{ M}$
$k_7 = 29ma \text{ s}^{-1}$	$b_c = 0.05 \text{ M}$

**Table 2** Experimental conditions in BZ-AOT systems and corresponding simulations parameters

	$h$ (M)	$a$ (M)	$c_0$ (mM)	$ma$ (M)	Ref.
Turing structures	0.2–0.225	0.15–0.2	4	0.225–0.3	14
	0.32	0.18–0.3	4 <sup>a</sup>	0.1–0.27	32
Accelerating waves	0.2	0.15	4	0.3	14
Spirals and antspirals	0.2	0.2–0.23	4	0.3	33
Packet waves	0.2–0.3	0.15–0.23	4	0.25–0.3	34
Segmented spiral waves	0.2	0.18	4.9 <sup>b</sup>	0.3	35
Oscillons	0.25	0.2	4.2 <sup>c</sup>	0.25	36
Jumping waves	0.18–0.2	0.18	4.9 <sup>b</sup>	0.3	37
Bubble waves	0.3	0.213	4.9 <sup>d</sup>	0.3	37
Rotating waves	0.2	0.18	4.9 <sup>b</sup>	0.3	37
Simulations parameters	0.1–0.3	0.1–1.2	1–6	0–15	

<sup>a</sup> [Ru(bpy)<sub>3</sub>]<sup>2+</sup> is used instead of ferroin. <sup>b</sup> Bathoferroin is used instead of ferroin. <sup>c</sup> Ferroin or [Ru(bpy)<sub>3</sub>]<sup>2+</sup> are used in these experiments. <sup>d</sup> Bathoferroin is used instead of ferroin and 0.067 M NaBr is added.

which light passes and the absorbance of the illuminated solution. The mathematical derivation of the photoactivation rate leads to a cumbersome expression.<sup>60</sup> Kádár *et al.* have obtained an experimental value of  $k(I) = 6.4 \times 10^{-6} \text{ s}^{-1}$ ,<sup>59</sup> but numerical simulations have also been performed with  $k(I) = 10^{-7}$ – $10^{-3} \text{ s}^{-1}$  and correctly reproduced experimental data.<sup>21,45</sup> Here we will consider  $k(I)$  as a freely controllable parameter comprized between 0 and 0.1 s<sup>-1</sup>. The photoinhibition term in eqn (2) and (3) has been derived by making the stationary state approximation for the excited catalyst Ru(II)\*.<sup>21,45</sup> Finally, this model does not distinguish between ferroin and the photosensitive catalyst, which means that the species M<sup>(n+1)+</sup> and M<sup>n+</sup> in the mechanism represent both catalysts at the oxidized and reduced states, respectively.<sup>21</sup> The full deterministic pFKN model has already been used in several simulations of microfluidic assemblies and provided results in accordance with experimental observations.<sup>21,23</sup> In the next section, we present the main features displayed by the model.

### 3 Deterministic analysis

In addition to a trivial state where the concentrations of all species are zero, the non-photosensitive system admits a single stationary state. The large number of parameters and the complexity of the equations give rise to a cumbersome analytical expression of this stationary state, which is thus not shown here. The photosensitive case generates similar features, with (a) a first state where all the steady concentrations are zero except for the catalyst, and (b) a non-trivial state. We performed numerical simulations of the evolution eqn (1)–(6) using a Python integrator for stiff equations (Isoda combined with bdf method). We also used AUTO-07p to detect critical points and compute bifurcation diagrams.<sup>61</sup> We first discuss the behavior of the system in the dark (*i.e.*, in the non-photosensitive case). The main goal of this section is to give an overview of the nonlinear dynamics generated exclusively by the chemistry of the BZ reaction. We also discuss the role played by certain species in the emergence of complex behaviors.

#### 3.1 The non-photosensitive BZ reaction

By analogy with experimental measurements, we show and discuss the properties of the concentration of the oxidized form of

the catalyst ( $z$ ) as a function of the concentration of malonic acid  $ma$ . The values attributed to parameters  $ma$ ,  $a$ ,  $h$  and  $c_0$  are compatible with experimental conditions (see Table 2), although we explored larger ranges of values for completeness.

We first discuss the general properties of the bifurcation diagram (see Fig. 1). At very low  $ma$  the non-trivial stationary state is stable but if  $ma$  increases the system undergoes a supercritical Hopf bifurcation (HB1), giving rise to oscillations. In the simplest cases, this transition leads directly to the oscillations described in the literature (see Fig. 3a).<sup>1,3</sup> The domain of existence of these oscillations is bounded by another supercritical Hopf bifurcation (HB2) located at larger  $ma$ . As can be seen in Fig. 1a and b, the domain of oscillations is significantly enlarged when  $a$  is increased, as a consequence of the displacement of HB2 to higher values of  $ma$ . The same trend is observed as  $h$  is increased.

Oscillations can also develop for  $ma < \text{HB1}$ . The presence of these oscillations can be explained on the basis of the bifurcation diagram shown in Fig. 2a. Starting from HB1, the stable orbit grows in amplitude as  $ma$  increases until a limit point (denoted LP1) is reached. A second limit point LP2 is detected at  $ma < \text{HB1}$  where large oscillations arise. A large amplitude orbit thus coexists with a stable stationary state between LP2 and HB1 and with another stable orbit (of smaller amplitude) between HB1 and LP1. This latter behavior corresponds to *birhythmicity*. In both cases, the initial conditions determine the effective

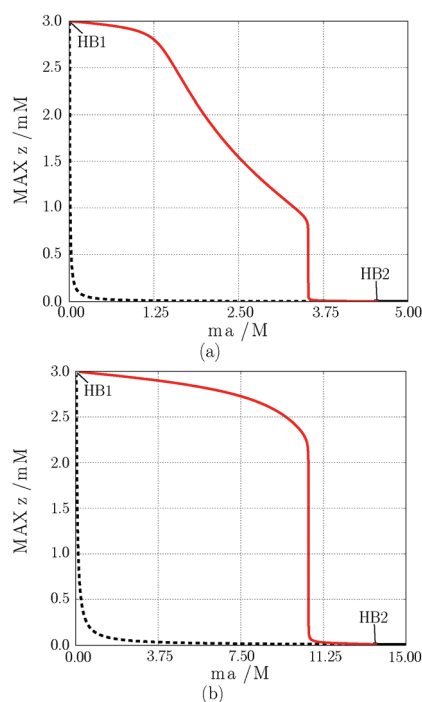


**Fig. 1** Bifurcation diagrams of  $z$  vs.  $ma$  for  $a = 0.3$  M (HB1 at  $ma = 2.661440 \times 10^{-3}$  M, HB2 at  $ma = 4.536620$  M) (a) and  $a = 0.9$  M (HB1 at  $ma = 2.746310 \times 10^{-2}$  M, HB2 at  $ma = 13.60630$  M) (b). The other parameters are  $h = 0.2$  M,  $c_0 = 3$  mM and  $k(l) = 0$  s<sup>-1</sup>. The plain lines correspond to stable stationary states while unstable trajectories are represented by dashed lines. The maxima of the oscillations are plotted in red and steady states in black.

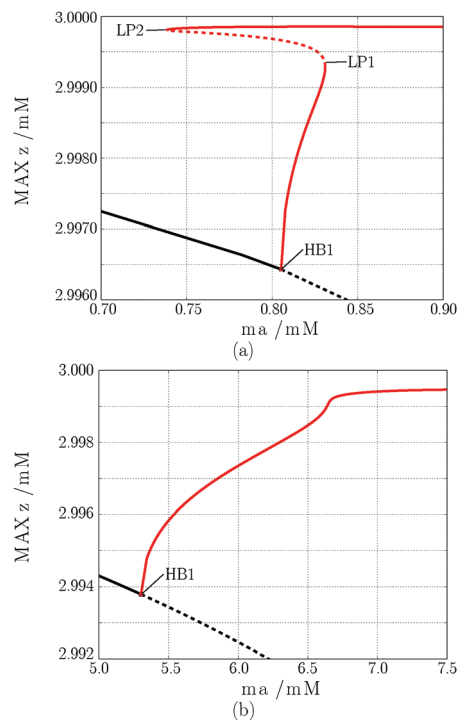


**Fig. 2** Bifurcation diagrams of  $z$  vs.  $ma$  for  $h = 0.1$  M (a) and  $h = 0.3$  M (b). The other parameters are  $a = 0.3$  M,  $c_0 = 3$  mM and  $k(l) = 0$  s<sup>-1</sup>. The plain lines correspond to stable stationary states while unstable trajectories are represented by dashed lines. The maxima of the oscillations are plotted in red and steady states in black.

regime chosen by the system. Birhythmicity has been observed in coupled BZ systems, experimentally<sup>62</sup> and theoretically,<sup>63</sup> but to the best of our knowledge, does not appear in individual BZ oscillators. As shown in Fig. 2b, the limit points disappear when the solution is more acidic ( $h$  is larger), in which case only simple oscillations can be found.

For values of  $a$  larger than those used in Fig. 1 and 2, the transition from the stationary state to the large amplitude oscillations involves even more bifurcations. Fig. 3a–d show how the simple periodic oscillations observed for  $ma > \text{HB1}$  are gradually transformed into multiperiodic oscillations by successive period doublings (PDs) as  $ma$  increases, until the trajectory finally becomes chaotic (see Fig. 3e). The complex, small amplitude oscillations arising from the PDs generally coexist with stable oscillations of large amplitude, as shown in the time series in Fig. 3f and as in the previous case of birhythmicity, the evolution of the system to one of these regimes depends on the initial conditions. These results are compatible with the episodes of multiperiodic oscillations and chaos reported in closed systems<sup>26</sup> and CSTR.<sup>57</sup> The range of initial concentrations leading to chaos is very narrow under the conditions of Fig. 3 but this domain widens if  $a$  increases. The bifurcation analysis shows that period doubling bifurcation points also appear when  $c_0$  is decreased.

For  $a = 1.2$  M, the system exhibits an additional interesting behavior which combines chaotic episodes and large amplitude oscillations. Very similar signals have been detected experimentally

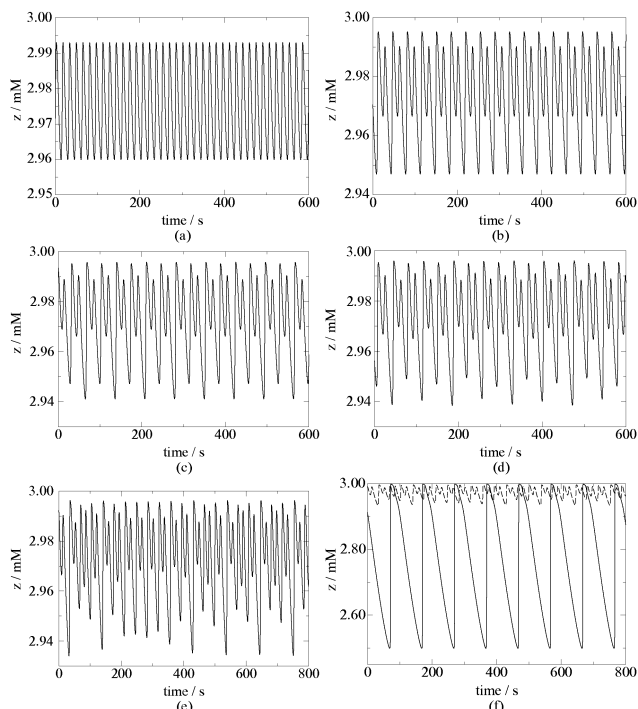


**Fig. 3** Asymptotic behavior of  $z$  vs.  $t$  for  $ma = 0.02960$  M (simple oscillations – P1) (a),  $ma = 0.02980$  M (biperiodic oscillations – P2) (b),  $ma = 0.02984$  M (quadriperiodic oscillations – P4) (c),  $ma = 0.02985$  M (octoperiodic oscillations – P8) (d),  $ma = 0.02986$  M and  $z_0 = 2.3 \times 10^{-3}$  M (chaos) (e) and  $ma = 0.02986$  M (simple oscillations of large amplitude) (f). In panel (f), the dashed line corresponds to the chaotic trajectory shown in panel (e). The other parameters are  $h = 0.2$  M,  $a = 0.9$  M,  $c_0 = 3$  mM and  $k(I) = 0$  s $^{-1}$ . Unless they are specified, the initial conditions are  $x_0 = 1 \times 10^{-6}$  M,  $y_0 = 5 \times 10^{-6}$  M,  $z_0 = 2.7 \times 10^{-3}$  M and  $u_0 = p_0 = w_0 = 0$  M.

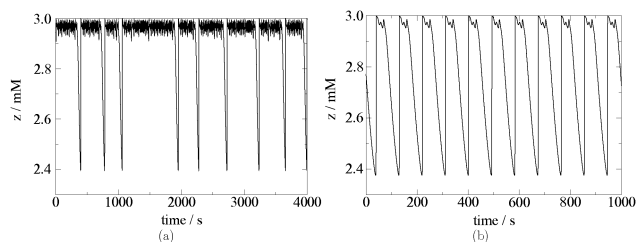


**Fig. 4** Asymptotic behavior of  $z$  vs.  $t$  for  $ma = 0.0546$  M (a) and  $ma = 0.0550$  M (b). The other parameters are  $h = 0.2$  M,  $a = 1.2$  M,  $c_0 = 3$  mM and  $k(I) = 0$  s $^{-1}$ . The initial conditions are  $x_0 = 1 \times 10^{-6}$  M,  $y_0 = 5 \times 10^{-6}$  M,  $z_0 = u_0 = p_0 = w_0 = 0$  M.

in a CSTR.<sup>27</sup> These oscillations are aperiodic (see Fig. 4a) in the neighborhood of the chaotic region but tend to become more regular and much more frequent (see Fig. 4b) for larger  $ma$ . Note that in the conditions of Fig. 4, multiperiodic oscillations and chaos do not coexist with another stable state or orbit, as can be seen on the bifurcation diagram in Fig. 5. As a consequence, these regimes can be observed whatever the initial conditions. If the domain of birhythmicity is enlarged, by reducing  $h$  for example, these complex oscillations are no longer observed.

In conclusion, the original FKN model generates a variety of nonlinear behaviors, ranging from simple oscillations to birhythmicity,

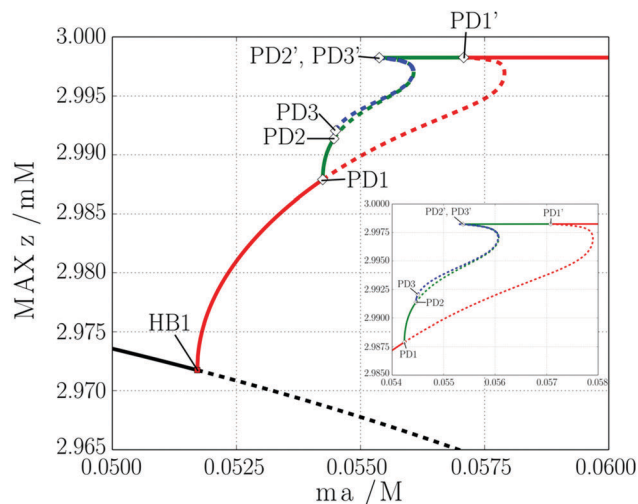


**Fig. 5** Bifurcation diagram of  $z$  vs.  $ma$  for  $h = 0.2$  M,  $a = 1.2$  M,  $c_0 = 3$  mM and  $k(I) = 0$  s $^{-1}$ . The inset is a zoom in the region of chaos and complex oscillations. The diamond symbols correspond to period doubling bifurcation points. The plain lines correspond to stable stationary states while unstable trajectories are represented by dashed lines. The steady states are in black while the maxima of the P1, P2 and P4 oscillations are respectively in red, green and blue. The P8 oscillations and further period doublings are not indicated for clarity.

**Table 3** Parameters to be tuned (increase  $\equiv$  +/decrease  $\equiv$  –) starting from the conditions of Fig. 2b to move HB2 or to observe LP and/or PD. The nonlinear behaviors affected by these changes are also indicated

	HB2 at larger $ma$	LP	PD multiperiodic	LP & PD
	larger oscillating	birhythmicity	osc. & chaos	complex osc.
	domain			
$h$	+	–		–
$a$	+		+	+
$c_0$			+	

chaos and complex oscillations and we identified the influence of some key parameters on the aforementioned regimes. It should be noticed that although the FKN model has been used and numerically integrated on numerous occasions, the above-mentioned complex behaviors (except for the simple oscillations) were not reported before. Table 3 summarizes how to tune the different parameters to observe a given dynamics, starting from the conditions of Fig. 2b, *i.e.*  $h = 0.3$  M,  $a = 0.3$  M,  $c_0 = 3$  mM and  $k(I) = 0$  s $^{-1}$ .

### 3.2 The photosensitive BZ reaction

The model presented in Section 2 accounts for the photoinhibition of oscillations by including a production term for bromide (the inhibitor) and for the oxidized catalyst. As mentioned before, this term involves three new parameters:  $k(I)$ ,  $b$  and  $b_c$ . This last parameter is fixed, while the value of  $b$  depends on the concentration of malonic acid and  $k(I)$  typically ranges from  $10^{-7}$  s $^{-1}$  to  $10^{-3}$  s $^{-1}$ .<sup>21,45</sup> Since the photoinhibition of the oscillations is more efficient at large light intensities, we expect the stability, the position and/or the size of the domain of oscillations to be affected by an increase of  $k(I)$ .

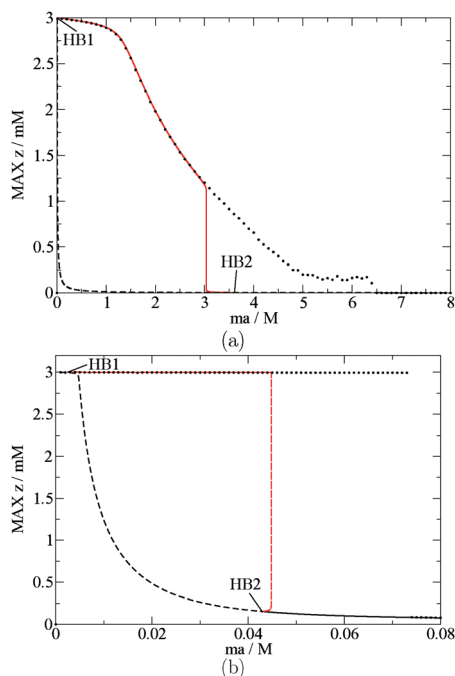


Fig. 6 Bifurcation diagrams of  $z$  vs.  $ma$  for  $k(I) = 10^{-5} \text{ s}^{-1}$  (HB1 at  $ma = 2.661170 \times 10^{-3} \text{ M}$ , HB2 at  $ma = 3.617130 \text{ M}$ ) (a) and  $k(I) = 10^{-3} \text{ s}^{-1}$  (HB1 at  $ma = 2.660970 \times 10^{-3} \text{ M}$ , HB2 at  $ma = 4.308540 \times 10^{-2} \text{ M}$ ) (b). The other parameters are  $h = 0.2 \text{ M}$ ,  $a = 0.3 \text{ M}$  and  $c_0 = 3 \text{ mM}$ . The plain lines correspond to stable stationary states and unstable trajectories are represented by dashed lines. The maxima of the deterministic oscillations are plotted in red and steady states in black. The black dots correspond to the results of stochastic simulations (maxima of the oscillations or steady states) performed with  $V = 5 \times 10^{-17} \text{ L}$ .

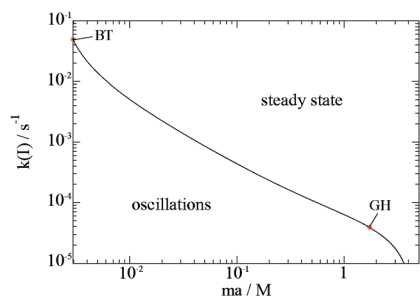


Fig. 7 2-Parameter bifurcation diagram: the black curve corresponds to the coordinates of HB2 in terms of  $k(I)$  and  $ma$  for  $h = 0.2 \text{ M}$ ,  $a = 0.3 \text{ M}$  and  $c_0 = 3 \text{ mM}$ . A Bogdanov-Takens bifurcation (BT) and a generalized Hopf bifurcation (GH) have also been detected. Oscillations are observed in the lower region of the diagram.

The bifurcation diagrams in Fig. 6a and b, corresponding respectively to  $k(I) = 10^{-5} \text{ s}^{-1}$  and  $k(I) = 10^{-3} \text{ s}^{-1}$ , show that the position of the first Hopf bifurcation (HB1) is barely affected by illumination (see also Fig. 1a). A similar conclusion also holds for the period doubling points. However, HB2 is dramatically reduced, especially for large  $k(I)$ , and the domain of oscillations is thus less extended. This trend is summarized in the 2-parameter bifurcation diagram of Fig. 7, where  $k(I)$  and the  $ma$  value corresponding to HB2 are plotted. For low  $k(I)$ , HB2

corresponds to relatively large values of  $ma$  and is a supercritical Hopf bifurcation, like in the non-photosensitive case. As  $k(I)$  increases, HB2 turns into a subcritical Hopf bifurcation point as the system goes through a generalized Hopf bifurcation (denoted by GH). This change can also be observed in the 1-parameter bifurcation diagrams (see Fig. 6a and b). Because of the subcritical character of HB2, large amplitude oscillations can coexist with a stationary state in a small neighborhood of HB2, for  $ma > \text{HB2}$ . This will reveal crucial to understand some of the behaviors observed with stochastic simulations (see Section 4). A Bogdanov-Takens (BT) bifurcation can also be found for even larger  $k(I)$ , signaling the disappearance of HB2 and thus of the domain of oscillations.

To summarize, light partially suppresses the oscillatory regime by displacing the second Hopf bifurcation point (*i.e.* oscillations survive at low  $ma$ ). We also detected two new codimension-two bifurcations in the model, namely the Bogdanov-Takens and the generalized Hopf bifurcations. In the next section, we discuss how this conclusion could be affected by intrinsic fluctuations.

## 4 Stochastic simulations

We simulated the fluctuating dynamics of the FKN model through the Gillespie algorithm, where a transition probability per unit time is associated to each reaction step (see ref. 64–67 for details). The extensivity parameter  $\Omega$  entering these probabilities is in our case obtained by  $\Omega = V \times N_A$ , where  $V$  is the volume (in L) of the water core of the micelle and  $N_A$  is the Avogadro number. Contrary to what happens when modeling a system with Langevin equations and simulations, noise is not simply introduced as additional terms to be included in the evolution equations. At each iteration, the reaction probabilities are calculated based on the current state of the system (*i.e.* the number of particles of each species). Two random numbers are selected from a uniform distribution. The first one is used in the selection of the reaction that will occur at this iteration and the second is involved in the calculation of the time elapsed before the next reaction. The number of molecules of each species are adapted accordingly to the stoichiometry of the selected reaction. Some details about the algorithm and the transition probabilities can be found in Appendix.

The two main parameters we tuned to act on the amplitude of fluctuations were  $V$  and the distance from the bifurcation points. The amplitude of fluctuations, as quantified by the ratio of the standard deviation of the number of particles and their mean ( $\sigma_n / \langle n \rangle$ ) is indeed expected to increase as  $\Omega$  decreases and/or as one approaches a critical point. As a consequence, we expect to recover the deterministic predictions in the macroscopic limit ( $\Omega \rightarrow \infty$ ) for systems operating far from bifurcation points, where fluctuations become negligible.

We investigated the influence of fluctuations for volumes ranging between  $10^{-18}$  and  $10^{-12} \text{ L}$ . These values are larger than the actual volume of the micelles used in experiments but  $V = 10^{-18} \text{ L}$  was the minimal volume required to observe

dynamics with a sufficiently long lifetime. This volume corresponds to approximately  $10^3$ – $10^4$  micelles. For smaller volumes, the reacting molecules are completely consumed in a very short time after ignition of the reaction and the system reaches the trivial stationary state. In the following paragraphs, we will first present the results obtained in the oscillatory, birhythmic and chaotic regimes of the non-photosensitive case and we will then focus on the stochastic dynamics under illumination.

#### 4.1 The non-photosensitive case

The parametric domain where oscillations can be found is larger in the presence of fluctuations (for the range of system size mentioned above). Indeed, oscillations can be found for  $ma$  much larger than the second Hopf point HB2. The reason behind this extension is that the steady state found for  $ma > \text{HB2}$  corresponds to a stable focus for a wide range of  $ma$ . What we observe thus corresponds to the well-known fluctuation-induced oscillations that are found beyond criticality in the case of “soft” supercritical Hopf bifurcations.<sup>68</sup> Fluctuations nevertheless perturb the period and sometimes the amplitude of the oscillations as illustrated in Fig. 8a. The variance of the period decreases as the size increases and is proportional to  $1/\Omega$ , as expected in the case of a simple limit cycle subjected to chemical noise.<sup>69,70</sup> The distribution of the period is Gaussian for “large” systems ( $10^{-16}$ – $10^{-15}$  L) but becomes more asymmetric for smaller systems.

The other complex dynamics prove to be much less robust to fluctuations. In the region close to HB1 where birhythmicity and chaos are expected in view of the deterministic analysis, the small amplitude oscillations and chaotic dynamics become hardly observable. More precisely, these behaviors become transients or intermittent regimes whose lifetime increases with the size of the system. This complex dynamics can be understood qualitatively as a succession of fluctuation-induced transitions between the basins of attraction of the different attractors that coexist in this parametric range. A typical transition from chaos to large amplitude oscillations is for example shown in Fig. 8b. The complex oscillations observed at  $a = 1.2$  M (see Fig. 4a) are transformed into an extremely noisy trajectory where chaotic episodes can no longer be distinguished from large amplitude oscillations. The chaotic

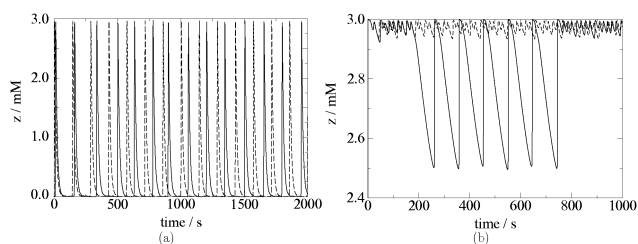


**Fig. 8** Time series of  $z$  for  $V = 10^{-18}$  L,  $a = 0.3$  M,  $ma = 0.6$  M and  $z_0 = 0$  M (a) and  $V = 10^{-14}$  L,  $a = 0.9$  M,  $ma = 0.02986$  M and  $z_0 = 0.0023$  M (b). The other parameters and initial conditions are  $h = 0.2$  M,  $c_0 = 0.003$  M,  $k(I) = 0$  s $^{-1}$  and  $x_0 = 1 \times 10^{-6}$  M,  $y_0 = 5 \times 10^{-6}$  M,  $u_0 = p_0 = w_0 = 0$  M. The plain line represents a stochastic realization while the dashed line is the corresponding deterministic trajectory.

intervals are more visible when the volume increases but remain much shorter than in the deterministic limit. It is only for volumes larger or equal to a given critical value (usually around  $V_c = 10^{-12}$  L) that all the deterministic trajectories are recovered.

We can thus conclude that for the non-photosensitive case, fluctuations tend to blur out most of the complex dynamical features observed in the deterministic limit of the FKN model. Only oscillations corresponding to a simple limit cycle seem to survive at small scales.

#### 4.2 The photosensitive case

Fluctuations tend to expand the domain of oscillations for the photosensitive system in a way similar to what was observed in the non-photosensitive case (see Fig. 6a). This expansion is particularly relevant for the efficiency of inhibition by light. In the deterministic limit, including the photoinhibition processes leads to a displacement of HB2 to lower  $ma$  values and thus to a shrinking of the domain of oscillations. As we just mentioned, this effect is however counterbalanced by fluctuations in small systems and photoinhibition is less effective in the presence of intrinsic noise.

New and unexpected phenomena can also be observed for large  $k(I)$ , when HB2 is subcritical in the deterministic limit. In this case, oscillations are expected to coexist with a stable steady state for a suitable choice of parameters. We observed that in this subcritical domain, there is an optimal system size for which the oscillations are more regular than in smaller and in larger systems. For small systems, fluctuations induce frequent transitions between the two attractors, which make the oscillations highly irregular, as expected. However, for large systems the frequency of oscillations also spreads widely (see Fig. 9a and b). The probability distribution of the period moreover tends to become much more asymmetric than for smaller volumes. Such situations correspond to time series in which reaction spikes are separated by periods of latency, during which the mean concentrations correspond to the stable stationary state (Fig. 9e). This can be explained by the fact that the intermittency involving the two attractors is due to fluctuations driving the system beyond the separatrix (red dashed line in Fig. 6b). When the amplitude of the fluctuations is reduced, these transitions are less frequent, but the time spent in each basin of attraction increases. For large systems, the dynamics will thus consist in long periods of oscillations followed by long phases of latency, and *vice versa*.

In comparison to the deterministic behavior, the range of  $ma$  for which the spikes are present is also much more extended (see Fig. 6b). As explained in Section 2, the oscillations are triggered when  $[\text{Br}^-] < [\text{Br}^-]_{\text{crit}}$ . If the amplitude of the fluctuations is sufficiently large (*i.e.*  $\sigma_c \geq \sigma_{c,\text{crit}}$ , where  $\sigma_c$  is the amplitude of the fluctuations of concentration), the fluctuations are very likely to induce such a perturbation in  $[\text{Br}^-]$ . The firing of a spike is thus expected to become less probable when the amplitude of the fluctuations is smaller. Indeed, the frequency of the spikes is reduced in larger systems or when the distance from HB2, located at  $ma \approx 0.555$  M for the conditions of Fig. 9, is increased. As shown by the histogram

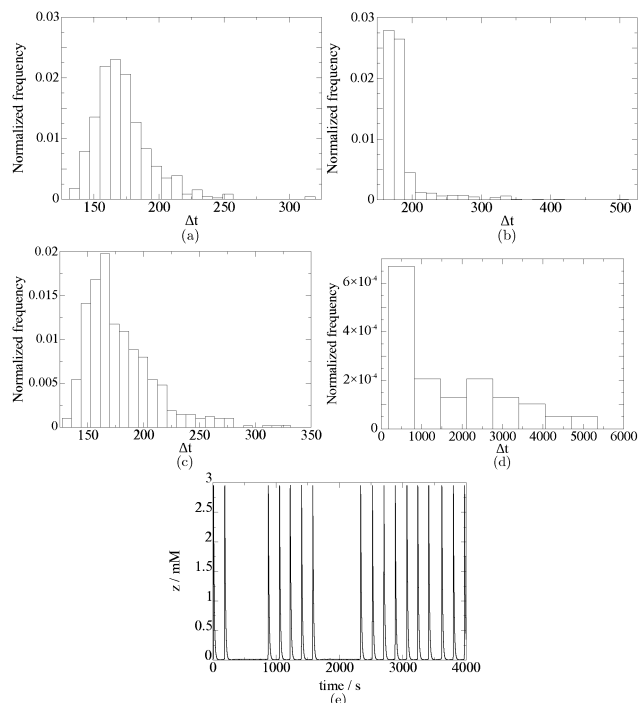


**Fig. 9** (a–d) Histograms of interspike time intervals for  $ma = 0.6$  M *i.e.* in the subcritical domain (a and b) and  $ma = 0.8$  M (c and d). (e) Time series of  $z$ . The other parameters and initial conditions are  $V = 10^{-17}$  L (a and c),  $2 \times 10^{-16}$  L (b),  $4 \times 10^{-16}$  L (d) or  $1 \times 10^{-15}$  L (e),  $h = 0.2$  M,  $a = 0.3$  M,  $c_0 = 3$  mM,  $k(l) = 10^{-4}$  s $^{-1}$  and  $x_0 = 1 \times 10^{-6}$  M,  $y_0 = 5 \times 10^{-6}$  M,  $u_0 = p_0 = w_0 = 0$  M.

in Fig. 9c, the mean interspike time interval is about 180 s and the maximal time interval between two spikes does not exceed 340 s for a volume of  $10^{-17}$  L. When the size of the system is increased, the number of spikes observed is much smaller and the interspike time intervals increase (Fig. 9d). The spikes eventually disappear when the size and the distance from the criticality are large enough to keep  $\sigma_c$  smaller than  $\sigma_{c,crit}$ . The trajectory then fluctuates around the deterministic stationary state.

To summarize, fluctuations strongly affect the nonlinear kinetics of the photosensitive model. The two effects discussed above both tend to extend the parametric domain where oscillations and similar behaviors can be found. The efficiency of inhibition by light is thus reduced for smaller systems.

## 5 Conclusions

We have studied the photosensitive FKN model with deterministic and stochastic simulations to analyze how fluctuations could affect the dynamics of the BZ reaction in small systems. We demonstrated that this model gives rise to a variety of nonlinear behaviors including simple oscillations but also, for the first time, multiperiodic oscillations, chaos and birhythmicity. Contrary to other models of deterministic chaos in the BZ reaction,<sup>71,72</sup> the (p)FKN model does not include a flow term characterizing the elimination of reactants and products. These results suggest that the chaotic dynamics is thus only the result of the chemical kinetics of the reaction performed in

a well-mixed reactor. Illumination enables the inhibition of oscillations by reducing the domain of oscillations, but cannot completely suppress all the complex dynamics in the range of parameters investigated.

In the presence of strong fluctuations, the simple periodic oscillations become less regular but are nevertheless much more robust than the more complex oscillations and chaos, which tend to be blurred out by the noise. Moreover, the efficiency of photoinhibition is strongly reduced in the presence of fluctuations, so that larger light intensities are required to annihilate oscillations.

These fluctuation-induced effects are negligible for the range of volumes used in microfluidic experiments and the deterministic approach is expected to describe correctly the chemical behavior of BZ droplets in this case. On the other hand, the chemical dynamics of a reaction occurring in a micelle could be dramatically modified by the intrinsic fluctuations. In most experiments, the number of micelles is of the order of  $10^{15}$  and since these nanoreactors constantly exchange reactants and products, depletion and other fluctuation-related phenomena should not be observed. However, for systems composed of a smaller number of micelles, the resulting collective behavior could be impacted by the individual fluctuating dynamics of the micelles. The role played by diffusion and collision–coalescence–redispersion processes in the synchronization of the nanoreactors could be assessed by simulating a small ensemble of stochastic micelles. In this way, one could analyze how the local fluctuation-induced phenomena translate into collective, spatio-temporal patterns.<sup>73</sup>

## Conflicts of interest

There are no conflicts of interest to declare.

## Appendix

### Transition probabilities

In the Gillespie algorithm, a propensity function is defined for each reaction step and depends on the kinetic constant and on the number of particles ( $n_x, n_y, \text{etc.}$ ) involved in the reaction. As mentioned before, the extensivity parameter is here defined by  $\Omega = V \times N_A$ , where  $V$  is the volume (in L) and  $N_A$  is the Avogadro number. At each iteration, a reaction and the time elapsed before the next reaction ( $\Delta t$ ) are selected randomly and the number of molecules of each species is adapted accordingly, *i.e.*  $n_i(t + \Delta t) = n_i(t) + \bar{\nu}_j$ , where  $\bar{\nu}_j$  corresponds to the number of molecules of species  $i$  produced ( $\bar{\nu}_j > 0$ ) or consumed ( $\bar{\nu}_j < 0$ ) during reaction  $j$ . For example, if the first reaction of Process A is selected,  $n_x(t + \Delta t) = n_x(t) - 1$ ,  $n_y(t + \Delta t) = n_y(t) - 1$  and  $n_p(t + \Delta t) = n_p(t) + 2$ . The selection of the reaction step  $j$  and the calculation of the time increment  $\Delta t$  involve the propensity functions  $\omega_j(\mathbf{n}) = c_j h_j(\mathbf{n})$ , where  $c_j$  depends on the kinetic constant of the reaction  $j$ ,  $\mathbf{n}$  is a vector containing the number of molecules of each species and  $h_j(\mathbf{n})$  gives the number of combinations formed with  $\mathbf{n}$  molecules reacting according to  $j$ .

Table 4 Propensity functions for the pBZ reaction

$\omega_1 = k_1 n_x n_y / \Omega$	$\omega_8 = n_8 n_p$
$\omega_2 = k_2 n_y$	$\omega_r = k_r n_w (n_w - 1) / \Omega$
$\omega_3 = k_3 n_x (n_x - 1) / \Omega$	$\omega_{\text{red}} = k_{\text{red}} n_w n_c \Omega$
$\omega_4 = k_4 n_x$	$\omega_9 = k_9 n_z$
$\omega_5 = k_5 n_y n_p / \Omega$	$\omega_{10} = k_{10} n_z$
$\omega_6 = k_6 n_u$	$\omega_I = k(I) n_c b / (b_c + b)$
$\omega_7 = k_7 n_u$	

For the pBZ reaction, the propensity functions can be found in Table 4. The transition probability  $b_j$  associated to a process  $j$  is then given by  $b_j = \omega_j(\mathbf{n}) / \omega(\mathbf{n})$ , where  $\omega(\mathbf{n}) = \sum_j \omega_j(\mathbf{n})$  is the total propensity function. The time increment  $\Delta t$  is given by

$$\Delta t = -\frac{\ln(r_1)}{\omega(\mathbf{n})} \quad (7)$$

and the reaction  $j$  is chosen such that

$$\sum_{i=1}^{j-1} \frac{\omega_i(\mathbf{n})}{\omega(\mathbf{n})} < r_2 \leq \sum_{i=1}^j \frac{\omega_i(\mathbf{n})}{\omega(\mathbf{n})}, \quad (8)$$

where  $r_1$  and  $r_2$  are random numbers uniformly distributed between 0 and 1.

## Acknowledgements

The work of I. G. K. is partially supported by the US National Science Foundation. V. V. acknowledges support from F.R.S.-FNRS PhD fellowship.

## References

- 1 A. F. Taylor, *Prog. React. Kinet. Mech.*, 2002, **27**, 247–325.
- 2 R. M. Noyes, R. Field and E. Körös, *J. Am. Chem. Soc.*, 1972, **94**, 1394–1395.
- 3 R. J. Field, E. Körös and R. M. Noyes, *J. Am. Chem. Soc.*, 1972, **94**, 8649–8664.
- 4 R. J. Field and R. M. Noyes, *J. Chem. Phys.*, 1974, **60**, 1877–1884.
- 5 R. Yoshida, S. Onodera, T. Yamaguchi and E. Kokufuta, *J. Phys. Chem. A*, 1999, **103**, 8573–8578.
- 6 S. Maeda, Y. Hara, R. Yoshida and S. Hashimoto, *Macromol. Rapid Commun.*, 2008, **29**, 401–405.
- 7 R. Yoshida, *Adv. Mater.*, 2010, **22**, 3463–3483.
- 8 I. R. Epstein, V. K. Vanag, A. C. Balazs, O. Kuksenok, P. Dayal and A. Bhattacharya, *Acc. Chem. Res.*, 2012, **45**, 2160–2168.
- 9 D. Winston, M. Arora, J. Maselko, V. Gáspár and K. Showalter, *Nature*, 1991, **351**, 132.
- 10 R. Tóth, V. Gáspár, A. Belmonte, M. C. O'Connell, A. Taylor and S. K. Scott, *Phys. Chem. Chem. Phys.*, 2000, **2**, 413–416.
- 11 D. Balasubramanian and G. A. Rodley, *J. Phys. Chem.*, 1988, **92**, 5995–5998.
- 12 I. Gonda and G. A. Rodley, *J. Phys. Chem.*, 1990, **94**, 1516–1519.
- 13 V. K. Vanag and D. V. Boulanov, *J. Phys. Chem.*, 1994, **98**, 1449–1453.
- 14 V. K. Vanag and I. R. Epstein, *Phys. Rev. Lett.*, 2001, **87**, 228301.
- 15 I. R. Epstein and V. K. Vanag, *Chaos*, 2005, **15**, 047510.
- 16 V. K. Vanag and I. R. Epstein, in *Self-Organized Morphology in Nanostructured Materials*, ed. K. Al-Shamery and J. Parisi, Springer Berlin Heidelberg, 2008, pp. 89–113.
- 17 T. Bãnsági, V. K. Vanag and I. R. Epstein, *Science*, 2011, **331**, 1309–1312.
- 18 I. R. Epstein, *Chem. Commun.*, 2014, **50**, 10758–10767.
- 19 M. Toiya, V. Vanag and I. Epstein, *Angew. Chem., Int. Ed.*, 2008, **47**, 7753–7755.
- 20 M. Toiya, H. O. González-Ochoa, V. K. Vanag, S. Fraden and I. R. Epstein, *J. Phys. Chem. Lett.*, 2010, **1**, 1241–1246.
- 21 J. Delgado, N. Li, M. Leda, H. O. González-Ochoa, S. Fraden and I. R. Epstein, *Soft Matter*, 2011, **7**, 3155–3167.
- 22 N. Tompkins, N. Li, C. Girabawe, M. Heymann, G. B. Ermentrout, I. R. Epstein and S. Fraden, *Proc. Natl. Acad. Sci. U. S. A.*, 2014, **111**, 4397–4402.
- 23 N. Li, J. Delgado, H. O. González-Ochoa, I. R. Epstein and S. Fraden, *Phys. Chem. Chem. Phys.*, 2014, **16**, 10965–10978.
- 24 N. Li, N. Tompkins, H. González-Ochoa and S. Fraden, *Eur. Phys. J. E: Soft Matter Biol. Phys.*, 2015, **38**, 1–12.
- 25 N. Tompkins, M. C. Cambria, A. L. Wang, M. Heymann and S. Fraden, *Chaos*, 2015, **25**, 064611.
- 26 J. Wang, P. G. Sørensen and F. Hynne, *J. Phys. Chem.*, 1994, **98**, 725–727.
- 27 J. L. Hudson and J. C. Mankin, *J. Chem. Phys.*, 1981, **74**, 6171–6177.
- 28 P. De Kepper, A. Rossi and A. Pacault, *C. R. Seances Acad. Sci., Ser. C*, 1976, **283**, 371.
- 29 P. Strizhak and M. Menzinger, *J. Phys. Chem.*, 1996, **100**, 19182–19186.
- 30 F. Argoul, A. Arneodo, P. Richetti and J. C. Roux, *J. Chem. Phys.*, 1987, **86**, 3325–3338.
- 31 A. N. Zaikin and A. M. Zhabotinsky, *Nature*, 1970, **225**, 535.
- 32 A. Kaminaga, V. K. Vanag and I. R. Epstein, *J. Chem. Phys.*, 2005, **122**, 174706.
- 33 V. K. Vanag and I. R. Epstein, *Science*, 2001, **294**, 835–837.
- 34 V. K. Vanag and I. R. Epstein, *Phys. Rev. Lett.*, 2002, **88**, 088303.
- 35 V. K. Vanag and I. R. Epstein, *Proc. Natl. Acad. Sci. U. S. A.*, 2003, **100**, 14635–14638.
- 36 V. K. Vanag and I. R. Epstein, *Phys. Rev. Lett.*, 2004, **92**, 128301.
- 37 A. A. Cherkashin, V. K. Vanag and I. R. Epstein, *J. Chem. Phys.*, 2008, **128**, 204508.
- 38 I. Z. Kiss, Y. Zhai and J. L. Hudson, *Science*, 2002, **296**, 1676–1678.
- 39 R. Toth, A. F. Taylor and M. R. Tinsley, *J. Phys. Chem. B*, 2006, **110**, 10170–10176.
- 40 A. F. Taylor, M. R. Tinsley, F. Wang, Z. Huang and K. Showalter, *Science*, 2009, **323**, 614–617.
- 41 V. Horvath, P. L. Gentili, V. K. Vanag and I. R. Epstein, *Angew. Chem., Int. Ed.*, 2012, **51**, 6878–6881.

- 42 G. Ghoshal, A. P. Muñuzuri and J. Pérez-Mercader, *Sci. Rep.*, 2016, **6**, srep19186.
- 43 A. P. Muñuzuri and J. Pérez-Mercader, *J. Phys. Chem. A*, 2017, **121**, 1855–1860.
- 44 K. A. Bold, Y. Zou, I. G. Kevrekidis and M. A. Henson, *J. Math. Biol.*, 2007, **55**, 331–352.
- 45 V. K. Vanag and I. R. Epstein, *J. Chem. Phys.*, 2009, **131**, 104512.
- 46 A. Kaminaga, V. K. Vanag and I. R. Epstein, *Angew. Chem., Int. Ed.*, 2006, **45**, 3087–3089.
- 47 V. K. Vanag, *J. Phys. Chem. A*, 1997, **101**, 7074–7084.
- 48 V. K. Vanag and I. Hanazaki, *J. Phys. Chem.*, 1995, **99**, 6944–6950.
- 49 L. Q. Zhou, X. Jia and Q. Ouyang, *Phys. Rev. Lett.*, 2002, **88**, 138301.
- 50 K. Miyakawa, T. Tanaka and H. Isikawa, *Phys. Rev. E: Stat., Nonlinear, Soft Matter Phys.*, 2003, **67**, 066206.
- 51 S. Kádár, J. Wang and K. Showalter, *Nature*, 1998, **391**, 770–772.
- 52 T. Amemiya, T. Ohmori, M. Nakaiwa and T. Yamaguchi, *J. Phys. Chem. A*, 1998, **102**, 4537–4542.
- 53 V. Beato, I. Sendiña Nadal, I. Gerdes and H. Engel, *Philos. Trans. R. Soc., A*, 2008, **366**, 381–395.
- 54 D. S. A. Simakov and J. Pérez-Mercader, *J. Phys. Chem. A*, 2013, **117**, 13999–14005.
- 55 A. Guderian, G. Dechert, K.-P. Zeyer and F. W. Schneider, *J. Phys. Chem.*, 1996, **100**, 4437–4441.
- 56 D. S. A. Simakov and J. Pérez-Mercader, *Sci. Rep.*, 2013, **3**, srep02404.
- 57 J. S. Turner, J. C. Roux, W. D. McCormick and H. L. Swinney, *Phys. Lett. A*, 1981, **85**, 9–12.
- 58 Y. Hara, H. Mayama and K. Fujimoto, *J. Phys. Chem. B*, 2014, **118**, 6931–6936.
- 59 S. Kádár, T. Amemiya and K. Showalter, *J. Phys. Chem. A*, 1997, **101**, 8200–8206.
- 60 V. K. Vanag, A. M. Zhabotinsky and I. R. Epstein, *J. Phys. Chem. A*, 2000, **104**, 8207–8215.
- 61 E. J. Doedel, Proceedings 10th Manitoba Conference on Numerical Mathematics and Computation, 1981, pp. 265–284.
- 62 I. S. Proskurkin, A. I. Lavrova and V. K. Vanag, *Chaos*, 2015, **25**, 064601.
- 63 C. G. Hocker and I. R. Epstein, *J. Chem. Phys.*, 1989, **90**, 3071–3080.
- 64 D. T. Gillespie, *J. Comput. Phys.*, 1976, **22**, 403–434.
- 65 D. T. Gillespie, *J. Phys. Chem.*, 1977, **81**, 2340–2361.
- 66 D. T. Gillespie, *Phys. A*, 1992, **188**, 404–425.
- 67 D. T. Gillespie, *Annu. Rev. Phys. Chem.*, 2007, **58**, 35–55.
- 68 P. Gaspard, *J. Chem. Phys.*, 2002, **117**, 8905–8916.
- 69 D. Gonze, J. Halloy and P. Gaspard, *J. Chem. Phys.*, 2002, **116**, 10997–11010.
- 70 C. Barroo, Y. De Decker, T. Visart de Bocarmé and P. Gaspard, *J. Phys. Chem. Lett.*, 2015, **6**, 2189–2193.
- 71 L. Györgyi and R. J. Field, *Nature*, 1992, **355**, 808–810.
- 72 R. J. Field, *Peregrinations from Physics to Phylogeny*, World Scientific, 2015, pp. 37–82.
- 73 J. Garcia-Ojalvo and J. Sancho, *Noise in Spatially Extended Systems*, Springer Science & Business Media, 1999.